Theoretical and experimental investigation on conformal polishing of microstructured surfaces

Pengfei Zhang[a], Zhao Jing[a], Saurav Goel[b,c], Xi Hou[d], Chunjin Wang[e], Chi Fai Cheung[e], Yebing Tian[f] and Jiang Guo[a*]

[a] *State Key Laboratory of High-performance Precision Manufacturing, Dalian University of Technology, Dalian, China*

[b] *School of Engineering, London South Bank University, London, SE10AA, UK*

[c] *Department of Mechanical Engineering, University of Petroleum and Energy Studies, Dehradun, 248007, India*

[d] *Institute of Optics and Electronics, Chinese Academy of Sciences, Chengdu, China*

[e] *State Key Laboratory of Ultra-precision Machining Technology, Department of Industrial and Systems Engineering, The Hong Kong Polytechnic University, Hong Kong, China*

[f] *School of Mechanical Engineering, Shandong University of Technology, Zibo, China*

* Corresponding author E-mail: guojiang@dlut.edu.com

Abstract: Microstructured surfaces are ubiquitous to various fields especially in lighting, diffuser devices and imaging systems. While the current precision machining technology can achieve conformal shapes, the finished quality of the machined surface cannot be assured. Addressing this issue, this paper proposes a conformal polishing method suitable to polish microstructured surfaces to achieve high surface quality while preserving the shape accuracy. As part of the investigations, the damping tool and profiling damping tool were developed for polishing the rectangular and cylindrical surfaces. The results showed that along the direction perpendicular to the profile of the micro feature, the distribution of the principal stress and velocity will change in different forms at the corner depending on the shape of the micro feature. The shape evolution model based on a single microfeature simulation was established by considering finite slip on the workpiece surface. The simulated surface shape accuracy after polishing agreed well with that obtained by the experiments. Moreover, pre-machining history such as the residual tool marks and burrs were effectively removed. The mean roughness (*R*a) of the rectangular structure was measured as 0.4 nm and that of the cylindrical structure was measured as 6.2 nm.

Keywords: Surface evolution, Shape accuracy, Microstructured surfaces, Conformal

polishing

1. Introduction

Microstructured surfaces find diverse applications in optics [1, 2]. Components such as diffuser [3], lens arrays [4, 5], and gratings [6, 7] contribute significantly to the field of illumination which benefits optical components [8, 9], imaging [10, 11] and light modulation [12, 13] to facilitate design of complex optical systems [14, 15]. As the performance requirements of optical instruments continue to push the technological limit, the demand for high-precision microstructured optical components is rising sharply [16, 17]. Consequently, innovative manufacturing methods to achieve nanoscale smoothness and submicron shape accuracy [18-20] are highly desirable.

Ultra-precision cutting and grinding are the two preferred methods in use currently to fabricate [21-23] microstructured surfaces but are limited by the level of finishing one can achieve. The complex microstructured surface with mean roughness (Ra) of 50 nm and shape accuracy of 0.65 μm was obtained by Wu et al. [24] through a five-axis machining system. Zhou et al. [25] fabricated annular microlens arrays on Si and 6H-SiC substrates using an integrated microcutting-etching method by combining single point diamond turning (SPDT) with ion beam etching (IBE). The surface roughness *R*a of microlens unit on Si obtained was 0.054 μm, and that on SiC was 0.011 μm.

Jiang et al. [26] processed microslot array, pyramid array and triangular pyramid array microstructured surfaces using an offset flying cutting servo system. The shape errors in the fabricated microstructured arrays were all below 1 μm. Guo et al. [27] fabricated V-groove microstructured surfaces using a single point diamond cutting process. The peak-to-valley (PV) shape accuracy of the V-shaped groove surface was less than 1μm and the surface roughness (Ra) was close to 15 nm.

It is known that the contact mode machining processes such as diamond machining leaves tool marks on the machined surface [28, 29], which were also observed in the investigations discussed above. While the displacement-controlled machining processes such as cutting, milling and grinding can attain high shape accuracy, they cannot assure good control on the machined surface quality [30, 31]. As a result, residual surface defects such as tool marks and burrs on the surface can compromise the performance of the components during their lifetime [32, 33]. For critical components such as optical diffuser, the residual marks left by the cutting tool causes optical interference that could lead to non-uniform brightness and small-angle scattering of light, consequently impacting the system resolution [34, 35]. For microstructured surface polishing, scholars have proposed the use of pin-type wheel-type tools [36, 37], abrasive jet polishing [38-40], magnetic field assistance [41, 42], laser polishing [43, 44] etc. However, these methods continue to pose the problems related to inferior quality of the polished surface [45, 46]. Moreover, traditional methods of polishing are only suitable for polishing sub-millimeter microstructured surfaces [47]. Also, the rapid degradation of the polishing tool leads to rapid wear during the direct contact with the workpiece. Most specifically, Jet polishing and magnetic field assisted polishing have been flagged to have the problems with left over of the residues of the abrasive particles [48] which causes shape errors and poor performance [49, 50]. Hence, the existing polishing methods are shrouded by the common problem that polishing tools are prone to wear which limits the ability to maintain the surface accuracy.

In recent years, non-contact polishing methods based on the shear thickening polishing (STP) principle have attracted a lot of attention due to the advantage of process flexibility [51, 52], ease of equipment preparation [53] and cost-effectiveness [54]. In recent time, Zhu et al. [51] carried out non-contact polishing using non-Newtonian fluid on the nickel matrix to obtain a smooth surface with a roughness (*R*a) of about 3.9 nm. Li et al. [55] employed a weak chemical shear thickening polishing process to polish spherical 9Cr18 parts and achieved an *R*a of about 25 nm with a PV shape accuracy of 1.16 μm. Wang et al. [56] polished Ti-6Al-4V biomaterial using chemistry enhanced STP method. A surface roughness *S*a of 7.2 nm was obtained while achieving a material removal rate of 118 nm/min.

Zhou et al. [57] proposed a magnetic field enhanced shear thickening polishing process to polish zirconia and achieved an *R*a of about 8.3 nm. The aforementioned studies demonstrate that the STP process has distinct advantages however, this method in the aforementioned investigations has only been applied to planar surfaces. In this regard, Li et al [58] developed an anhydrous-based shear thickening slurry to polish KDP surfaces and achieved an Ra of 1.37 nm. Zhang et al. [59] developed a damping tool to polish aspherical surfaces of nickel-phosphorus alloy and reported an Ra of less than 1 nm.

It can once again be seen that the use of STP has been attempted only on flat [60, 61] and curved surfaces [62, 63] and its full potential to polish microstructured surfaces is yet to be unveiled.

Clearly, the utilisation of non-contact method based on STP method by employing non-Newtonian fluids presents significant advantages to finish optical components at scale. Hence, this approach can also be extended to facilitate ultra-precision polishing of microstructured surfaces. Owing to the distinctive geometric attributes of these microstructured surfaces, characterized by a substantial depth-to-width ratio, there exists a need for sub 10 nm surface roughness while preserving shape accuracy [64, 65].

Addressing this issue was the major motivation of this paper. Consequently, a damping tool and a profiling damping tool for finish machining of microstructured surfaces were developed as part of this investigation. A shape prediction model based on a single microfeature simulation considering finite slip on the workpiece surface was also developed. The result shows that the distribution of the principal stress and velocity, which determine the material removal during the polishing process, changes irregularly with the change of the microstructured surface profile. The experimental results showed that the shape error after polishing was less than 1 μm such that the surface roughness of the diffuser mold converges to 6.2 nm while the roughness of the grating surface decreases to 0.4 nm.

2. Research methodology

The material removal principle used in this study is based on the shear-thickening effect of non-Newtonian fluids [66, 67], and the damping tool and profiling damping tool were purposely designed to achieve effective polishing of microstructural workpieces at different depth scales. The polishing tool consists of a tool base and a damping pad (see Fig 1). The damping pad is affixed to the tool surface to enable effective driving of the polishing slurry. Due to the presence of the damping layer, the slurry can be stably driven by the designed tool, quickly reaching the peak of the thickening curve and fluctuating in the highest viscosity region. Under the high-speed shearing action of the tool, the slurry of the workpiece surface thickens, and the material in the form of microfeatures gets removed by the particle clusters formed during the process.

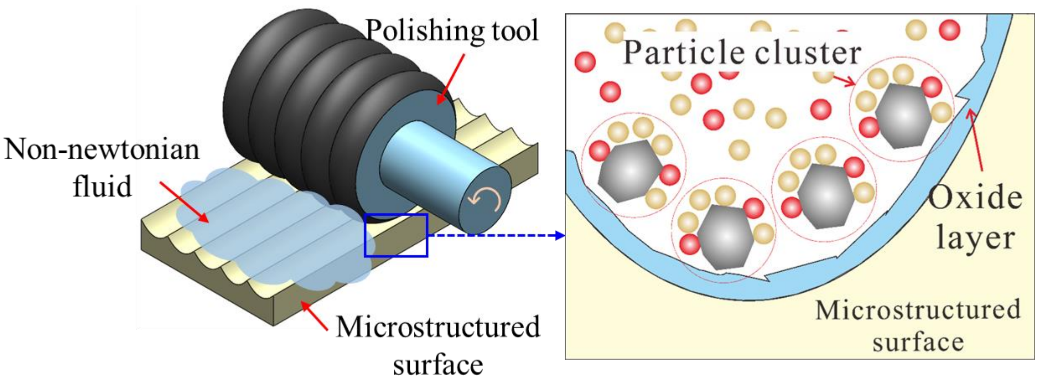

Fig. 1. Schematic of the material removal principle.

The damping and profiling damping tools were designed to polish the microstructured surfaces across different scales. When damping tools were used to polish structures with depths of about hundreds of micronmeters, the microfeature bottom was always unable to obtain effective material removal. Damped profiling tools have been developed for polishing microstructures with depths about hundreds of micrometers. It should be noted that the profiling damping tool is specifically designed for array V-grooves and cylindrical structures and is not compatible with structures that have vertical sides, such as rectangular structures. Damping tools were developed for polishing the microfeatures with depth of about a few or tens of micrometers. The damping tool consists of a cylindrical base and a damping cloth. The function of the damping cloth is to drive the polishing slurry effectively. Profiling damping tools were developed for polishing the microfeature with depth of about hundreds of micrometers. The profiling damping tool consists of a tool base, a soft film and a damping cloth. The profiling damping tool ensures a constant gap between the tool and the microfeature profile, thereby removing the workpiece surface material as evenly as possible.

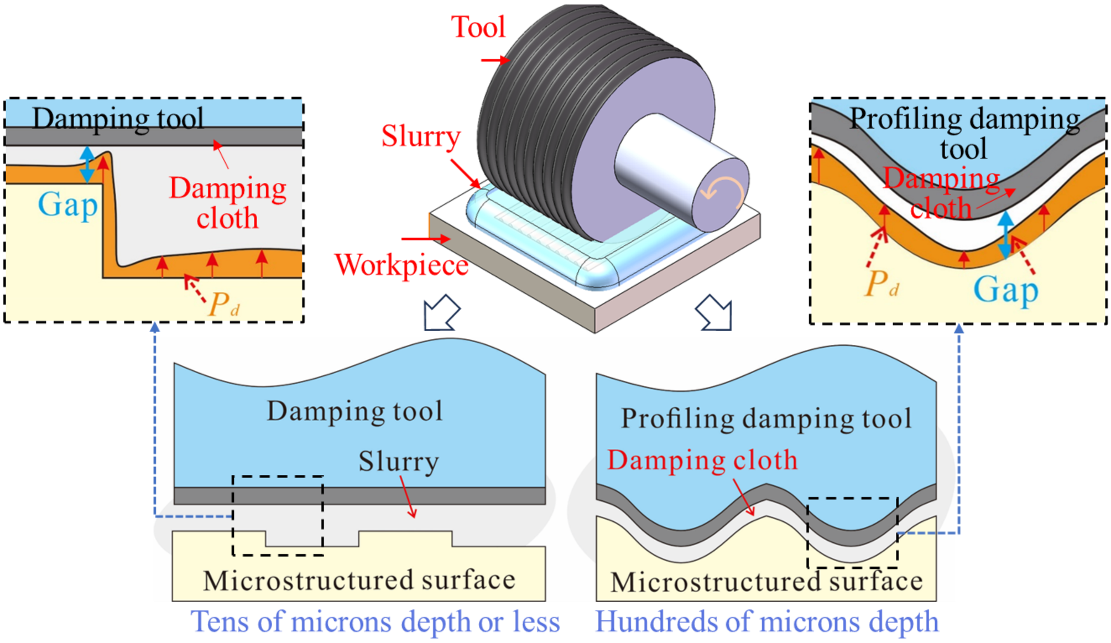

Fig. 2. Schematic diagram of the conformal polishing method.

3. Modelling and simulation

In this section, to find out the pressure and velocity field during the polishing process and the material removal distribution on the microstructured surface workpiece, CFD is used to simulate the polishing process and a material removal model based on the simulation is established. The rheological properties of the polishing slurry and the finite slip condition of the workpiece surface are considered in the simulation process. Based on the simulated surface pressure and velocity fields, a material removal model was established to predict the surface shape of the microstructured surface during polishing.

3.1. Finite element method

In the finite element modeling process, the workpiece surface was set to finite slip [68]. Fig. 3 shows the velocity distribution in the gap under no slip and finite slip conditions, and the distribution of slurry velocity u and shear force τ in the working gap. The workpiece surface slip velocity U_s can be expressed as

$$U_w = \begin{cases} 0, & \tau < \tau_c \\ U_s \left(\dfrac{\tau - \tau_c}{\tau_n} \right)^m \exp\left(-\dfrac{BP}{\tau_n} \right), & \tau > \tau_n \end{cases} \quad (1)$$

where τ_n and τ_c are normal and critical stresses respectively, m is a positive power, B is a pressure coefficient and P is pressure [69, 70].

In most cases, the pressure coefficient is minimal and in processes such as extrusion and lubrication flow of viscoplastic fluids and extrusion of polyethylene, the contribution from this term can be ignored [71]. Therefore, the pressure coefficient B was set as 0 for the simulation in this paper. The exponent m could be 1 or larger. Based on these experimental results and also to simplify the model, the positive power m was set as 1.5 and the τ_n and τ_c were both set to be 5000 Pa based on the experimental results when the smooth state of the workpiece surface is utilized. The value of U_s was changed to simulate different magnitudes of slip.

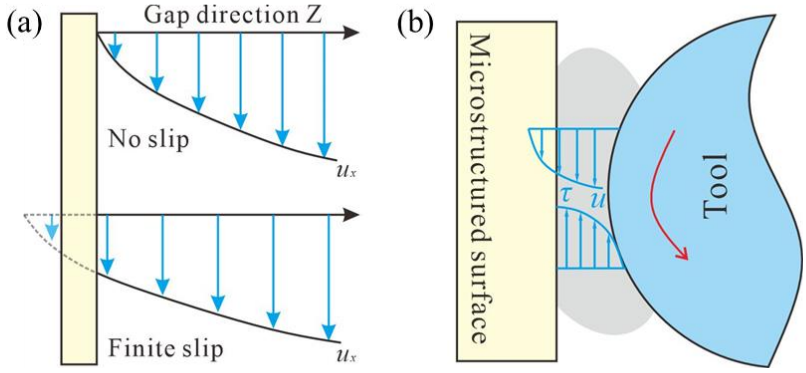

Fig. 3. Schematic diagram of (a) non-slip and finite slip, (b) velocity and shear stress field in the working gap under finite slip condition.

The finite element software ANSYS CFX was used to solve the pressure and velocity field of microstructured surface in wedge gap during polishing [72]. Fig. 4 show the relationship between the tool and the workpiece as well described the boundary conditions adopted for simulating the polishing process. Fig. 4(a) shows the fluid domains between a single microfeature and the tool, taking the profiling damping tool as an example. The tool surface was set to have no slip wall and the workpiece surface was set to have a finite slip wall. The top region of the fluid domain was set as open boundary, and the side region was set as symmetric boundary. The fluid domain was meshed with tetrahedral elements. In addition, all relevant parameters used in the simulation process are shown in Table 1. the consistency coefficient was set as 0.62 Pa s, the initial shear rate was set as 0.001 s^{-1}, the peak shear rate was set as 120 s^{-1}, the viscosity index was set as 1.5 and the density of the fluid was set as 1450 kg/m^3.

Table 1

Parameters set in the simulation model

Parameters	Value
Initial shear rate γ_i	0.001 s^{-1}
Peak shear rate γ_p	120 s^{-1}
Consistency coefficient K	0.62 Pa s
Slurry density ρ	1450 kg/m^3
Pressure coefficient B	0
Positive power m	1.5
Normal stresses τ_n	5000 Pa
Critical stresses τ_c	5000 Pa
Working gap d	0.2 mm
Tool speed n	600 rpm
Tool diameter D	30 mm

As shown in Fig. 4(b), the cross-sectional view of the surface meshing of single rectangular and cylindrical microfeatures, the wedge-shaped gaps were meshed entirely. Figure 4(c) shows the geometric dimensions of the tool and workpiece surface set during the simulation modeling process.

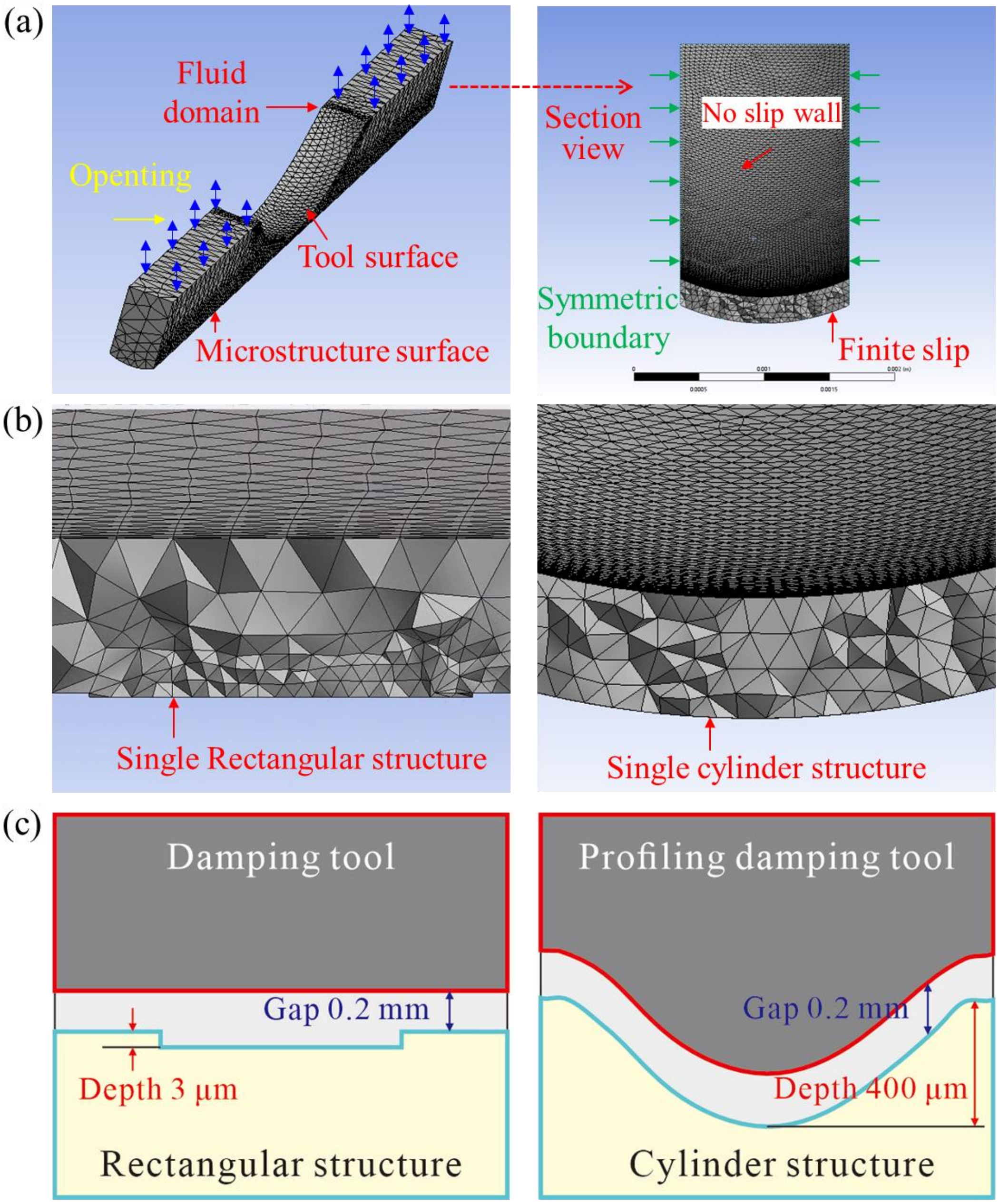

Fig. 4. (a) boundary conditions set in the simulation and (b) grids and (c) geometry size in the model.

3.2. Shape prediction model

In this section, the processing TIF and material removal distribution are modeled based on the matrix data obtained from the simulation to predict the surface shape of the polished microstructured surface.

3.2.1. Calculation of TIF

TIF function is an important part of deterministic polishing. Usually, the footprint of TIF is related to the pressure on the surface of the workpiece during polishing and the speed of the abrasive particle movement relative to the surface of the workpiece [73, 74]. When the pressure on the workpiece surface exceeds a certain threshold, the material yields and is removed at the same time. Similarly, the material removal in this work is related to the pressure and velocity on the nickel-phosphorus alloy material surface. But the difference is that this pressure is determined by the principal stress P_p induced by the dynamic pressure p_d and shearing stress τ. The speed is determined by the speed of the particle relative to the surface of the workpiece.

According to the von-Mises criterion [75], the equivalent principal stress P_p considering the shear stress can be estimated as

$$P_p(x,y) = \sqrt{p(x,y)^2 + 3\tau(x,y)^2} \tag{2}$$

where $p(x,y)$ and $\tau(x,y)$ are the dynamic pressure and shear stress field in the wedge gap.

The velocity field (V) was exported from the simulation model. Given the distribution of principal stress and velocity, the TIF matrix (R) can be estimated based on Preston's law[76] and $R(x,y)$ can be expressed as

$$R(x,y) = K \cdot P_p(x,y) \cdot V(x,y) \tag{3}$$

3.2.2. Surface removal distribution calculation on microstructured surfaces

By determining the dwell time of the tool on the workpiece surface as shown in Fig. 5, the material removal distribution of the microfeature surface was obtained by Eq. (4) [77, 78].

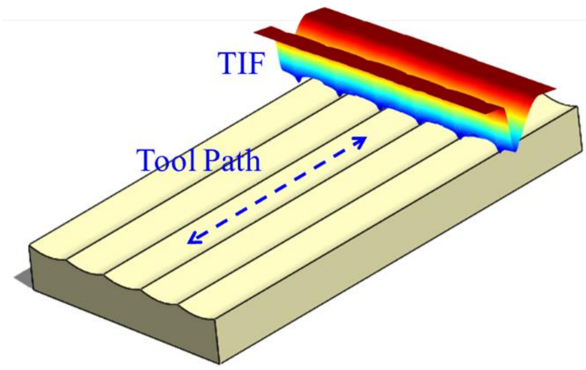

Fig. 5. Tool path diagram.

$$\begin{aligned} E(x,y) &= R(x,y) ** T(x,y) \\ &= \int_{-\infty}^{\infty}\int_{-\infty}^{\infty} R\left(x-x', y-y'\right) T\left(x', y'\right) dx' dy' \end{aligned} \tag{4}$$

where $R(x,y)$ is the TIF of the polishing tool at the dwell point and the dwell time distribution can be written as $T(x,y)$.

The discrete form of material removal distribution can be expressed as

$$E(x,y)=\sum_{i=0}^{I}\sum_{j=0}^{J}R\left(x-x_i',y-y_j'\right)T\left(x_i',y_j'\right)\Delta x'\Delta y' \tag{5}$$

where, I and J are the sampling points parallel to the X and Y directions of the workpiece respectively.

The matrix solution method was used to transform the two-dimensional convolution equation into a matrix equation for solving, so formula (5) can be written in a matrix form as

$$[E]_{i\times 1}=[R]_{i\times j}[T]_{j\times 1} \tag{6}$$

Therefore, the material removal distribution matrix [E]i×1 can be expressed as

$$\begin{bmatrix} e_1 \\ e_2 \\ \vdots \\ e_i \end{bmatrix}=\begin{bmatrix} r_{11} & r_{12} & \cdots & r_{1j} \\ r_{21} & r_{22} & \cdots & r_{2j} \\ \vdots & \vdots & \ddots & \vdots \\ r_{i1} & r_{i2} & \cdots & r_{ij} \end{bmatrix}\begin{bmatrix} t_1 \\ t_2 \\ \vdots \\ t_j \end{bmatrix} \tag{7}$$

3.3. Prediction procedure

Fig. 6 show the flowchart of the shape accuracy prediction process. The dimensions of the microfeature depth used for polishing were measured and the damping tool or the profiling damping tool was selected based on whether its depth is tens or hundreds of microns. In the CFD simulations, the tool speed n, and working gap h based on the material properties of the non-Newtonian fluid slurry were used as inputs. The space between the workpiece and the microfeatures was defined as the fluid domain, the boundary conditions of the model were defined, and the workpiece surface was set as finite slip wall. Then, the steady state simulation of the fluid flow was carried out and the calculation terminated when RMS converged to e^{-5}. At the end of the calculation, the post-processing was performed and the velocity and Von Mise stress value were extracted to calculate the TIF of a single microfeature surface. The material removal distribution was estimated based on the dwell time of the tool on the microstructured surface of the workpiece. Finally, the profile and error of the machined workpiece surface were estimated (see Fig 6).

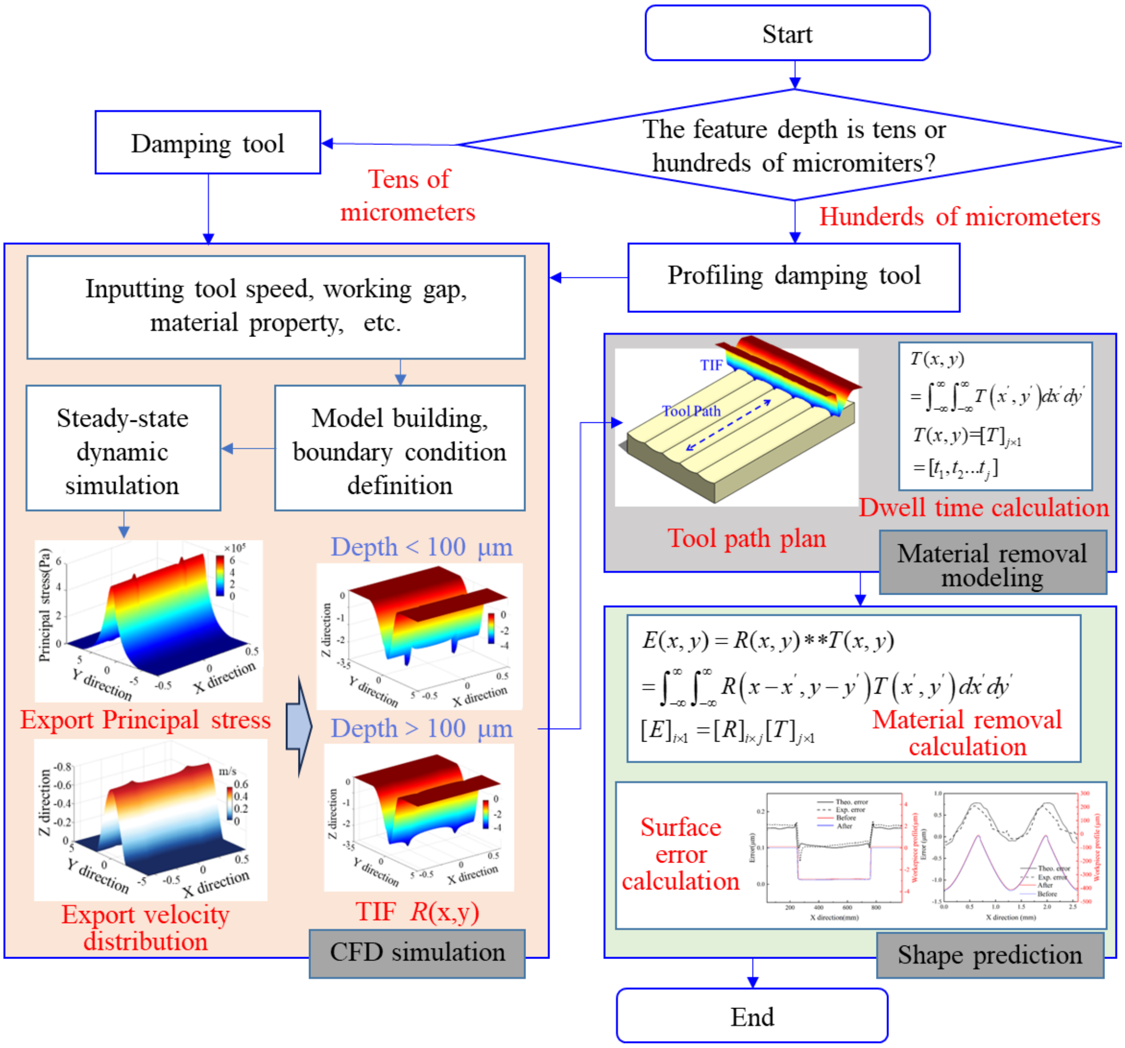

Fig. 6. Flow chart of surface shape prediction.

4. Equipment and process parameters

In this section, the workpiece material object for basic experiment, the production process of polishing tools and the specific test equipment used are introduced in detail. In addition, the polishing slurry used in this experiment and the process parameters are also described in detail.

4.1. Materials

In this study, the microstructured surface in a nickel-phosphorus alloy was obtained by ultra-precision milling process for basic experiments (see Fig 7). Fig. 7(a) shows a rectangular micro featured workpiece with a depth of about 3 μm and a period of 1 mm. Fig. 7(b) show a cylindrical microfeature workpiece with a depth of about 400 μm and a period of 1 mm.

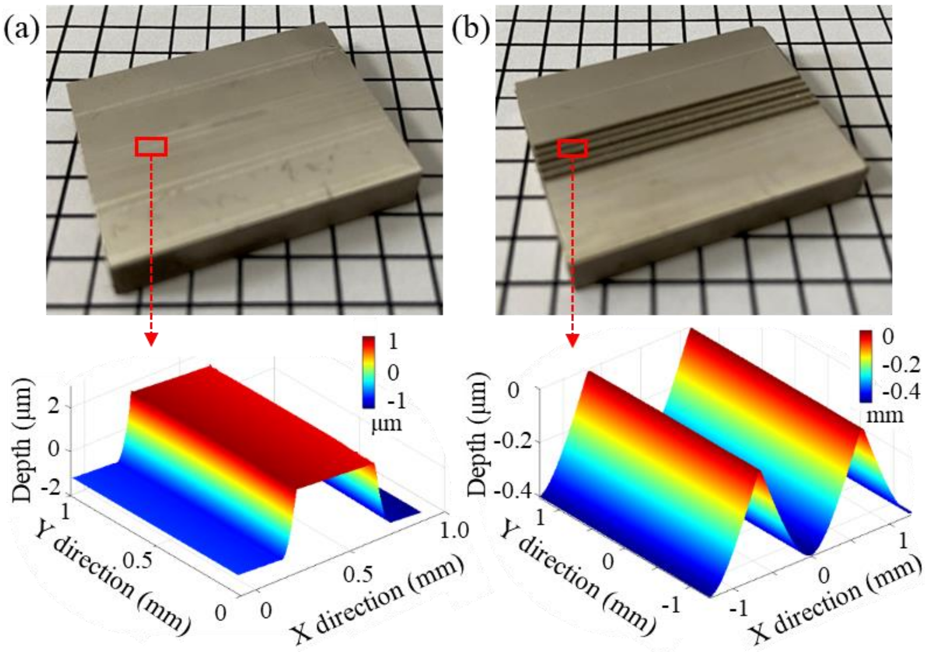

Fig. 7. (a) Rectangular and (b) cylindrical microstructured workpiece prepared for the experiment.

4.2. Tool design and fabrication

The damping tool and the profiling damping tool were designed to polish the microstructured surfaces. In contrast to the damping tool, the profiling damping tool requires a series of sequences to complete the production of the tool, before carrying out the experiment. Fig. 8 depicts the schematic diagram of the fabrication process of the profiling damping tool. Before conducting the polishing experiment, the initial step involved aligning the polishing tool body parallel to the surface of the workpiece. In the second step, the polishing tool was raised to a distance of 0.2 mm above the workpiece surface in preparation for the profile replication. In the third step, the molten glue was injected into the gap while rotating the tool body, and the profile of the workpiece was copied. The fourth step was to trim the excess film produced by replication and the prefabricated area used to bond the damping pad. In the fifth step, move the profiling damping tool to the gap of 0.2 mm above the workpiece, and the profiling damping tool production and position adjustment were completed.

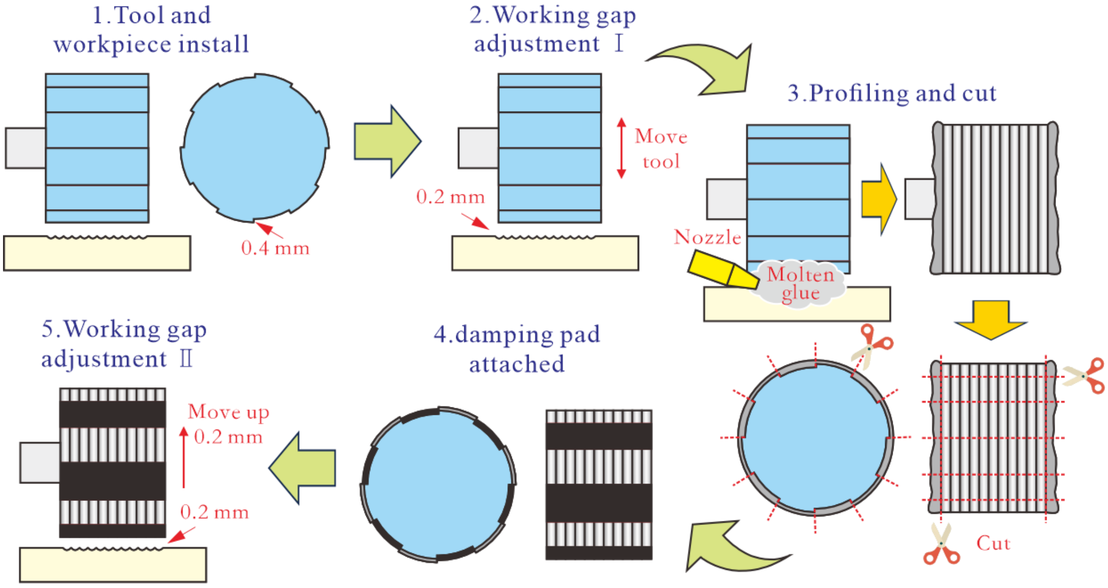

Fig. 8. Profiling damping tool fabrication procedure.

Fig. 9(a) shows a damping polishing tool prepared for microstructured surface polishing with depth of about tens of micrometers or less. The tool surface can be seen to be covered by a damping cloth, and due to the presence of the damping cloth, the polishing slurry can be driven steadily to remove the material efficiently. Fig. 9(b) shows the profiling damping tool, whose surface is covered by equally spaced duplicated structure film and damping cloth.

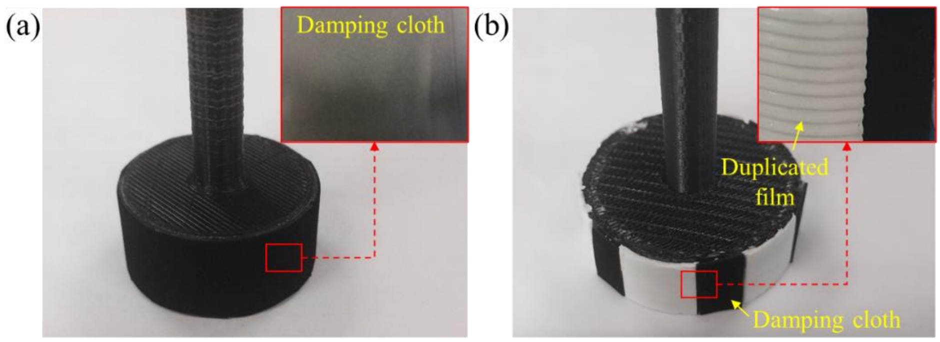

Fig. 9. The prepared (a) damping tool and (b) profiling damping tool.

4.3. Experimental setup and procedure

The polishing test was carried out on the self-developed 5 degree of freedom (DOF) precision machining platform as shown in Fig. 10. The spindle installed with the polishing tools can be adjusted between 0 and 90° as required, and the rotating shaft installed with the workpiece can be adjusted to the specified angle between the workpiece and the horizontal plane according to actual needs. The relative position of the workpiece and the polishing tool can be adjusted by moving the XYZ axis. The slurry is transported to the polishing interface through the nozzle by the self-made blade pump, and it returns to the collection pool through the tank. During the polishing process, the tool axis is first set parallel to the surface of the workpiece and then the tool is moved to a gap of 0.2 mm above the workpiece for the profiling procedure, and finally, the tool position is adjusted by moving the profiling damping tool to 0.2 mm above the workpiece. During polishing, the workpiece is fed reciprocally along the Y-axis, the feed speed is set to 1 mm/min, and the tool speed is set to 400-600 rpm. The slurry employed in this study is a mixture of non-Newtonian fluid and silica sol. The non-Newtonian fluid consists of a polyhydroxyl polymer and deionized water. The abrasive size and concentration of SiO_2 are 50 nm and 10%, respectively.

Table 2

Composition of the polishing fluid and processing parameters during polishing

Composition	Content	Parameters	Value
Abrasive (SiO_2)	10 wt%	Working gap	0.2 mm
Multi-Hydroxyl Polymer	52 wt%	Tool speed	600 rpm
Oxidant	6.5 wt%	Feed rate	100 mm/min
Deionized Water	31.5 wt%	Tilt angle	0°
		Tool diameter	30 mm

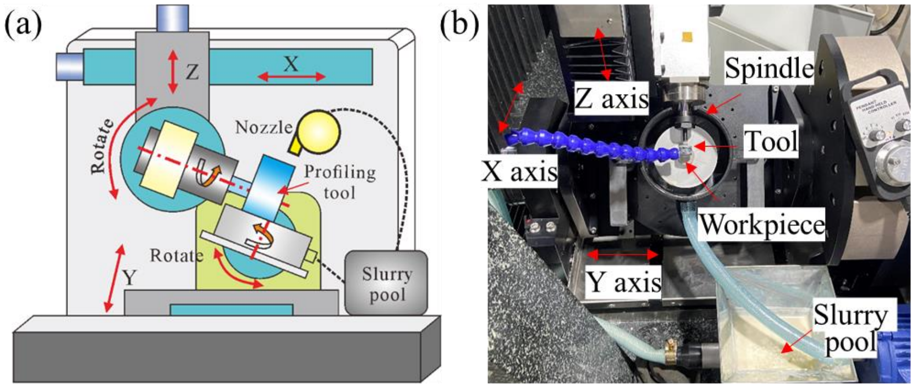

Fig. 10. (a) Schematic and (b) actual experimental set up.

4.4. Measurement equipment and method

The surface morphology of NiP alloy was observed using a super depth of field microscope (VHX-600E03041132, KEYENCE, Japan) before and after polishing. The three-dimensional topography and roughness of the workpiece surface were measured by a white light interferometer (NewView9000, Zygo, USA). The objective lens used for measurement is 10× (Zygo), the measurement and analysis range both are 400×400 μm. The roughness was evaluated using the arithmetic mean deviation (*Ra*), using a Gaussian high-pass filter with a cut-off length of 80 μm. The surface profile of the workpiece was measured using a Taylor contact profilometer (Form TalySurf PGI 840, Taylor Hobson, UK).

5. Results and discussion

The simulation and experimental results are described and discussed in detail in this section. Firstly, the velocity vector distribution of microstructured surface obtained under the no slip and finite slip conditions are introduced. At the same time, the principal stress and velocity field of rectangular and cylindrical structured surfaces obtained by simulation are also introduced. Then the TIF of the proposed method and the simulation results are discussed. The results of surface shape prediction after polishing are compared with the experimental results, and the surface formation process during polishing is illustrated. Finally, the condition before and after polishing of the object workpiece and its surface roughness are shown and discussed.

5.1. Velocity fields comparison

Fig. 11 shows the velocity field and velocity vector distribution in the simulated wedge gap and workpiece surface, where the workpiece surface was set as no slip wall and finite slip wall respectively. Fig. 11(a) shows the velocity field in the fluid domain obtained when the workpiece surface was set with a no-slip boundary condition. As depicted in the Fig. 11, two vortices with decreasing speed were seen to form at both ends of the wedge gap. The velocity vector within the wedge gap aligns parallel to the linear velocity direction of the tool surface. It gradually diminishes from the tool surface towards the workpiece, eventually reaching a velocity of 0 at any given point on the workpiece surface. In Fig. 11(b), the velocity field within the fluid domain was obtained when the workpiece surface was configured with finite slip conditions. Different from the no-slip state, the surface speed of the workpiece gradually decreases with the increase of the working gap, and the velocity direction in the gap is parallel to the tool rotation direction, and the velocity of the workpiece surface is about 0.7 m/s. The results show that using the finite slip boundary condition on the workpiece surface can reveal results close to the experimental results.

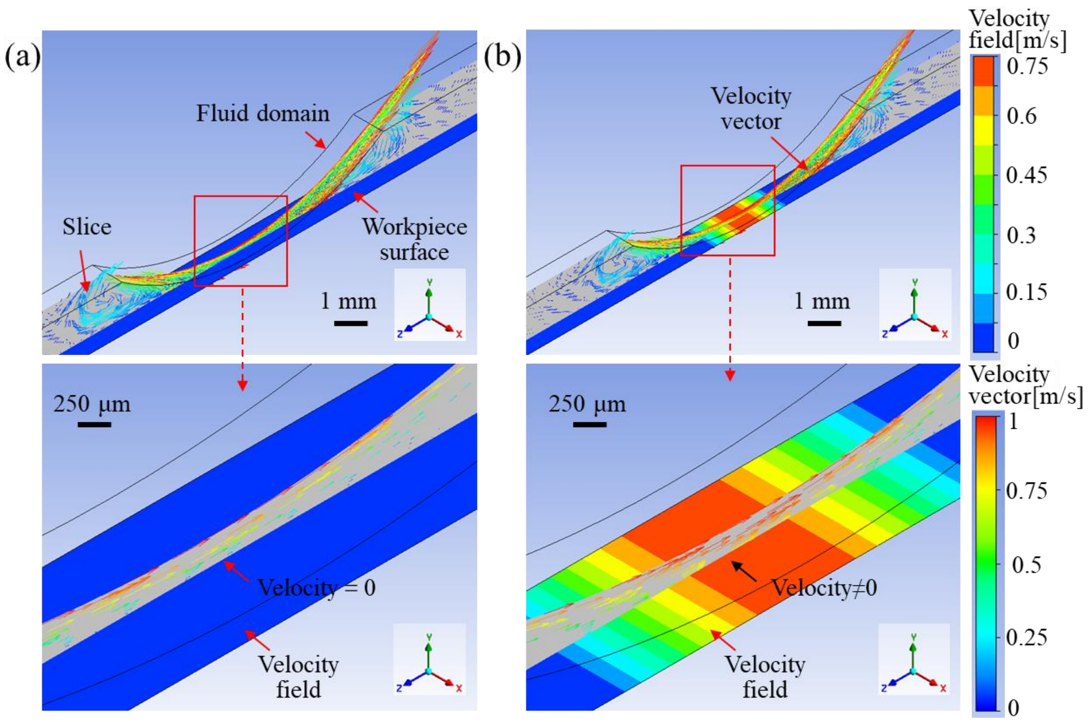

Fig. 11. Velocity field of (a) no-slip and (b) finite slip surface.

5.2. Principal stress and velocity fields on microstructured surface

For microstructured surfaces, surface pressure and velocity determine the material removal and uniformity, so it is crucial important to find out the distribution of principal stress and pressure on the microstructured surfaces. In this section, the principal stress and velocity distributions of flat, rectangular and cylindrical structures obtained by finite element simulation and modeling are analyzed, and the main factors affecting material removal are revealed and verified.

Flat workpiece was firstly applied in simulation and modeling programs. Figure 12 shows the principal stress and velocity field on flat workpiece surface. Figure 12(a) shows the relative position diagram of the tool and the workpiece. The workpiece is flat in this part. Figure 12 (b) shows the distribution of the principal stress on the workpiece surface obtained by simulation, and Figure 12 (c) shows the cross section of the principal stress distribution. As shown in the figure, on the flat surface, the principal stress field demonstrate V-shaped in the Y direction, and the workpiece surface is subjected to the greatest principal stress at the narrowest gap position. Figure 12 (d) shows the velocity field on the flat surface, and Figure 12 (e) shows the cross section of the velocity distribution. As shown in the figure, the velocity distribution has a similar trend as the principal stress, showing a V-shaped distribution, and the maximum velocity is found at narrowest gap position. Figure 12(f) shown an interpretation diagram of the principal stress and velocity distribution on the flat surface. The pressure and velocity are uniformly distributed.

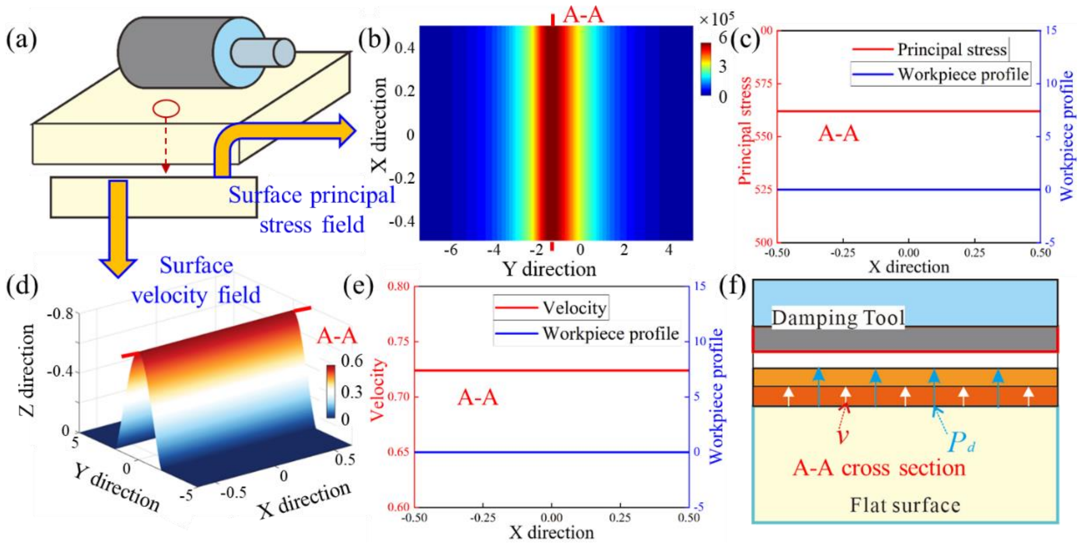

Fig. 12 Diagram of (a) relative position, (b)(c) principal stress, (d)(e) velocity distribution, and (f) interpretation on flat surface.

Rectangular structure is further performed in simulation and modeling programs. Fig. 13 shows the distribution of principal stress and velocity on the rectangular microstructured surface obtained by simulation. Figure 13 (b)(c) shows the distribution of the principal stress and cross section on the rectangular workpiece surface. On the rectangular microstructured surface, the principal stress field is also demonstrating V-shaped in the Y direction of the workpiece. However, as can be seen from the cross-section diagram, in the vertical direction of the microfeature (X direction), the principal stress field changes at the edges and corners of the microfeature. The phenomenon of increased principal stress was found at the corner of the convex, the velocity reduction phenomenon was found at the corner of the concave part. Figure 13 (d)(e) shows the distribution of the velocity and cross section on the rectangular workpiece surface. As shown in the figure, the velocity distribution of the rectangular structure also changes at the corners of the micro features, but unlike the principal stress, the velocity shows a decreasing trend at the convex corners. Figure 13(f) is a schematic illustration of this pressure and velocity variation.

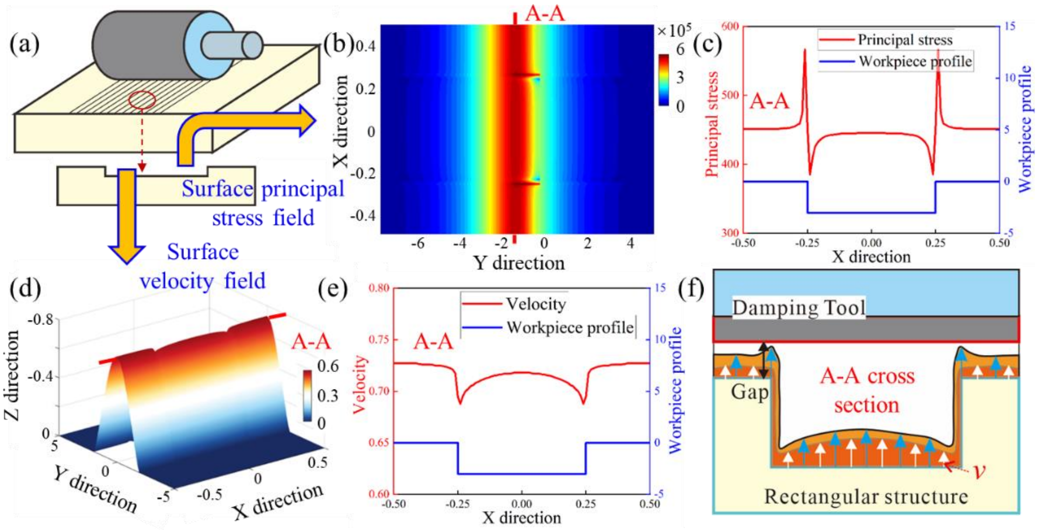

Fig. 13 Diagram of (a) relative position, (b)(c) principal stress, (d)(e) velocity distribution, and (f) interpretation on rectangular surface.

Cylindrical structure is alse performed in simulation and modeling programs. Figure 14 shows the principal stress and velocity field on the cylindrical microstructured surface using profiling damping tool obtained by simulation. Figure 14 (b)(c) shows the distribution of the principal stress and cross section on the cylinder micro feature. Similar to flat and rectangular structures, the principal stress distribution along the X direction is V-shaped. the principal stress field also changes at the corners of the microfeature. The maximum principal stress distribution is found at the corner of the end of the cylinder. Figure 14 (d)(e) shows the distribution of the velocity and cross section on the cylinder micro feature. The velocity distribution along the X direction is also V-shaped. The maximum velocity is also found at the end of the cylindrical structure. Figure 14(f) is a schematic illustration of this pressure and velocity variation. As can be seen from the figure, the maximum principal stress and velocity are both concentrated at the end of the cylindrical structure. This means that more material removal occurs at the end of the cylinder, which is discussed in the next section.

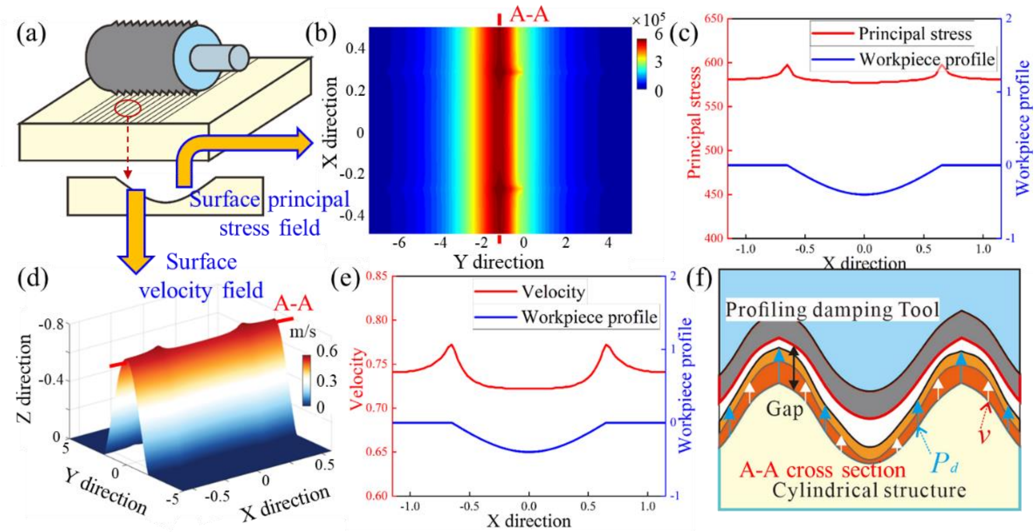

Fig. 14 Diagram of (a) relative position, (b)(c) principal stress, (d)(e) velocity distribution, and (f) interpretation on cylindrical surface.

5.3. Tool influence function

Fig. 13 shows the simulated TIF when polishing the flat, single rectangles, and cylindrical surface. The TIF distribution was calculated from Eq. (6). Fig 13 reveals that on the flat surface, there is a V-shaped TIF distribution, with the largest material removal occurring at the narrowest wedge gap on the workpiece surface. When dealing with rectangular or cylindrical microfeatures, uneven material removal can be observed at the corners of these microfeatures. When the structural feature is rectangular (about a few microns), most material gets removed at the sharp corners of the convex part of the microfeature and relatively less material removal was observed at the sharp corners of the concave part of the microfeature, and relatively less material removal occurred at the sidewall area of the microfeature. For structural features that are cylindrical (about hundreds of microns), the surface of the microfeatures undergoes relatively consistent material removal, with slightly increased material removal occurring at the corners of the microfeatures.

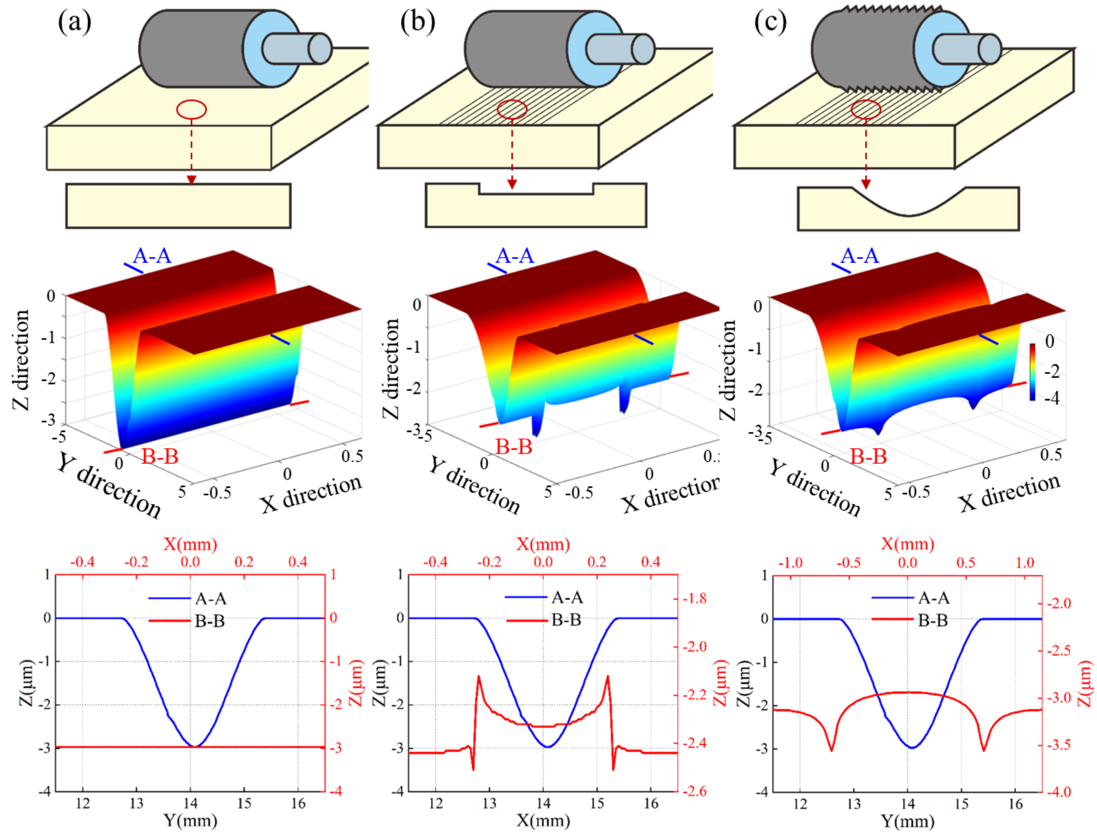

Fig. 15. TIF for single (a) flat, (b) rectangular, (c) groove structured surface.

5.4. Accuracy of the profiling damping tool

To find out the accuracy of the tool during the process of polishing, the profile of the profiling damping tool was measured. Fig 14 shows the contour of the tool and the workpiece. It can be observed from Fig 14 that the tool profile overlaps closely with the profile of the workpiece. There is only a slight deviation between the depth of the tool and the workpiece, and this deviation is mainly reflected in the convex part of the tool. The specific deviation value was about 30 μm, which may be caused by the cooling contraction of the film after replication. The working gap in the polishing process was 0.2 mm, and this deviation of the tool is far less than the working gap, so the impact on the polishing process can be negligible.

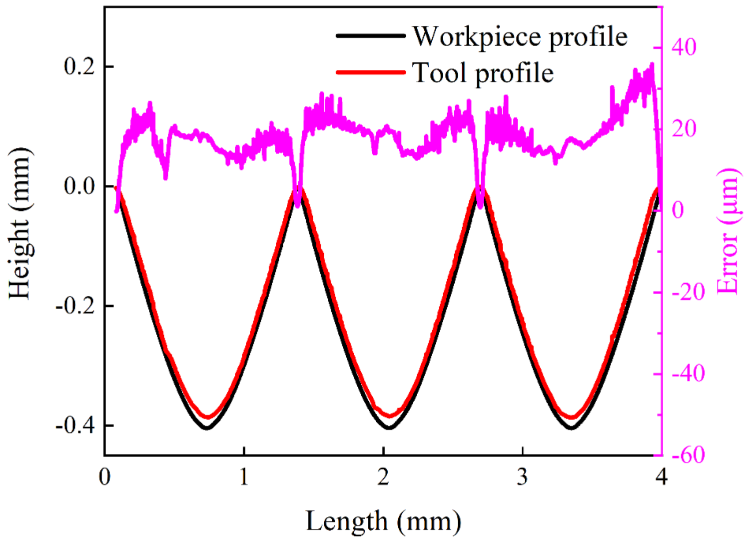

Fig. 16. The profile error between the profiling damping tool and the workpiece.

5.5. Shape accuracy

To find out the surface shape accuracy of the rectangular and cylindrical structures after polishing, the profile of the microstructured surface workpiece before and after polishing was measured. Fig 15 shows the calculated surface shape errors of rectangular and cylindrical structures before and after polishing. The results show that the theoretical and experimental results were consistent. As depicted in Fig 15(a), the error before and after polishing of the rectangular structure was about 0.2 μm. The maximum material removal occurred on the top corner of the rectangular structure, while lesser material removal occurred on the bottom corner of the rectangular structure, which can explain the reason for the edge roll-off of the rectangular structure.

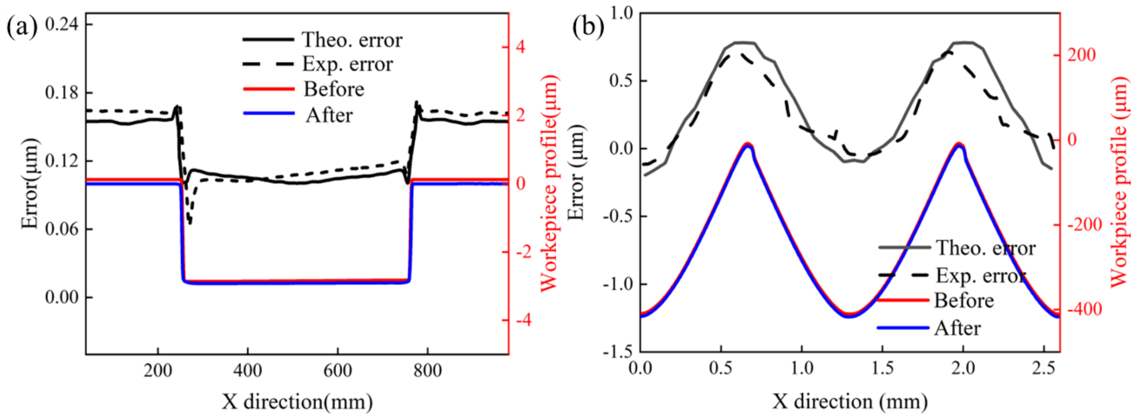

Fig. 17. Theoretical and experimental errors of single (a) rectangular and (b) cylindrical microstructured surfaces.

5.6. Surface quality

To further verify the effectiveness of the proposed tool and the non-contact conformal polishing method, the grating rectangular microstructured workpiece was prepared for the polishing experiments. Fig 16 shows the surface observation image and quality of grating rectangular before and after polishing. Fig 16(a) and (b) depict microscopic images of the microstructured workpiece surface before and after the polishing process. Noticeable color streaks resulting from diffraction can be observed on the surface before polishing, but they disappear after the polishing process. Significant differences in brightness were observed between the top and bottom surfaces before polishing, and these differences disappeared after the polishing. In addition, many parallel tool marks and burrs produced by cutting were observed on the rectangular microfeature surface. After polishing, the surface became smoother while the defects were eliminated, and the roughness decreased from the initial *R*a 2.1 nm to 0.4 nm (see Fig 16(c)).

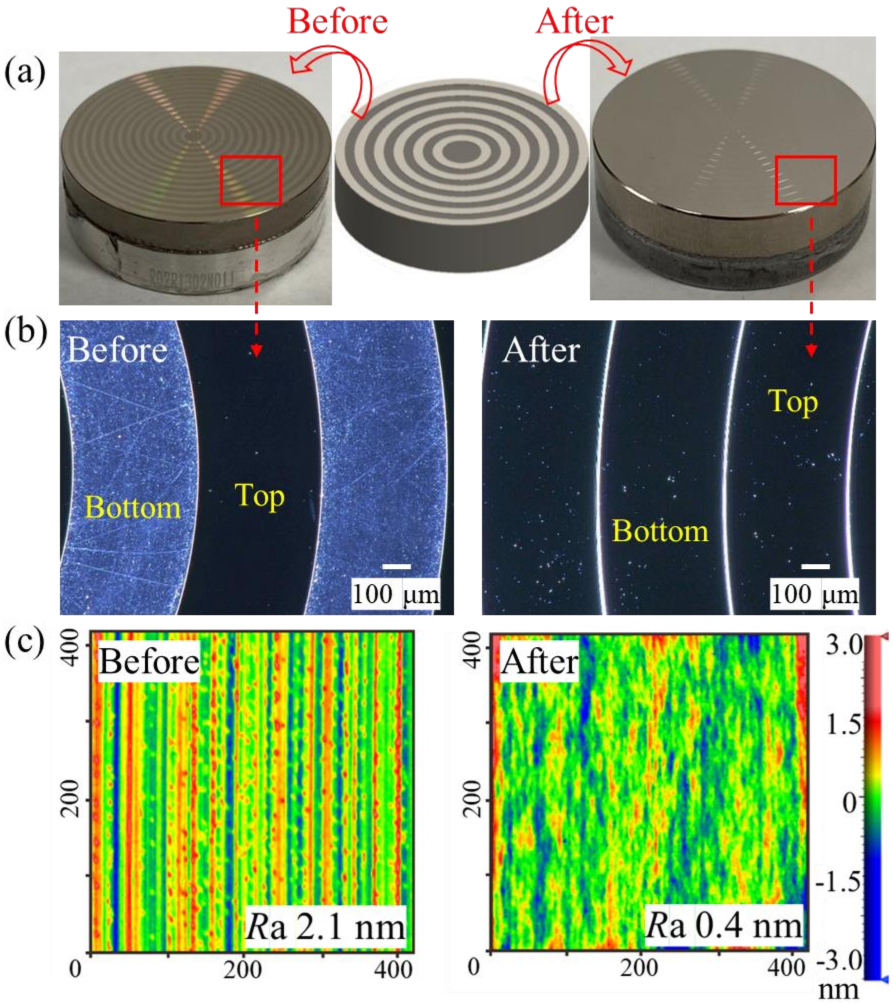

Fig. 18. Surface (a) observation (b) microscopic image and (c) roughness of grating rectangular surface before and after polishing.

Fig 17 shows the surface image and roughness results of the diffuser mold before and after the polishing. Fig 17(a) and (b) show the images of the workpiece before and after polishing. Many spiral tool marks and burrs were found on the diffuser mold surface before polishing. After polishing, the surface of the mold microfeature became smooth and most of the tool marks and burrs on the surface were eliminated. Fig 17(c) shows the surface roughness of the mold before and after polishing. The surface roughness was about 94.2 nm *R*a before polishing, and the surface roughness reduced to 6.2 nm *R*a after polishing for 1 hour, which decreased by 93.4%.

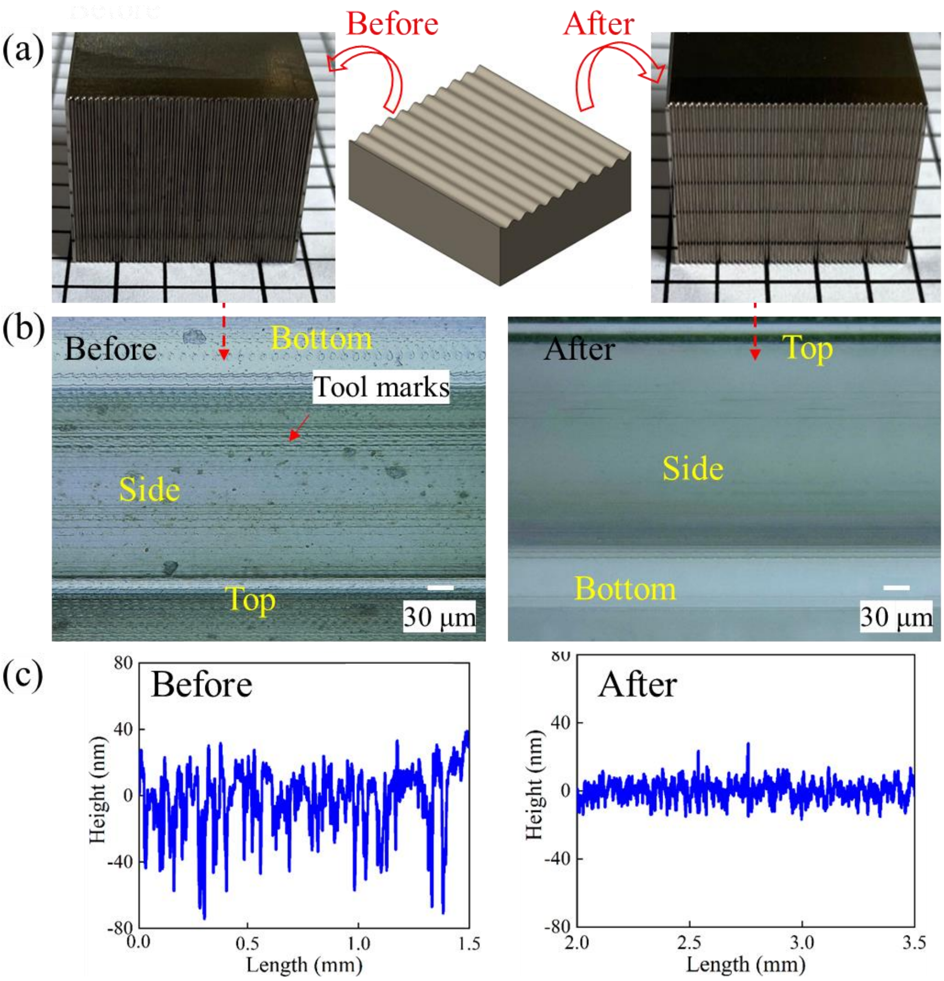

Fig. 19 Surface (a) observation (b) microscopic image and (c) roughness of diffuser mold before and after polishing.

6. Conclusions

In this paper, a non-contact conformal polishing method using self-developed polishing tools to finish microstructured surfaces is proposed. The material removal and shape evolution of the workpiece surface at different scales were investigated using an integrated simulation and experimental approach. The broad conclusions can be summarized as follows:

A new damping tool to polish microstructured surfaces at depth of about a few or tens of micrometers and a profiling damping tool to polish at depth of about hundreds of micrometers were developed. These two polishing tools are demonstrated to be industrially useful for polishing array structures with complex shapes. The associated error between the profiling damping tool and the workpiece profile was below 30 μm.

Simulation considering the finite slip between the workpiece and the slurry was configured. The pressure and velocity fields on the microfeature surface were studied. Larger von Mises stress distribution and larger material removal were seen to happen on the sharp corners of the top and bottom of rectangular structures and the corners of cylindrical microfeatures.

A surface shape prediction model based on the simulation of single microfeature was established. The proposed model accurately predicted the shapes of both rectangular and cylindrical structures after polishing, demonstrating strong corroboration with the experimental results. The shape error of the polished array rectangle and cylindrical structure were about 0.3 μm and 0.8 μm, respectively.

The surface quality of the grating and diffuser mold taken as a testbed study was improved significantly after polishing. The surface defects such as tool marks and burrs on the workpiece surfaces were effectively eliminated. The surface roughness of the grating has seen an 84% decrease reaching 0.4 nm, while the surface roughness of the diffuser mold has decreased by 93% to 6.2 nm.

Acknowledgements

The authors gratefully acknowledge the financial support provided by the Funds for International Cooperation and Exchange of the National Natural Science Foundation of China (No. 52311530080), the National Natural Science Foundation of China (No. 51975096). In addition, the authors would also like to acknowledge the financial support provided by the Royal Society through the International exchange Cost Share award (IEC\NSFC\223536).

Appendix A. The solving process NS equation in finite element model

To describe slurry flow mathematically, governing equations [79] related to the conservation of mass and momentum in the fluid are applied. These equations can be written in three dimensions

Mass conservation equation (Slurry continuity)

$$\frac{\partial u}{\partial x}+\frac{\partial v}{\partial y}+\frac{\partial w}{\partial z}=0 \tag{8}$$

Momentum conservation equation

$$\frac{\partial p}{\partial x}=\frac{\partial}{\partial z}\left[\mu\frac{\partial u}{\partial z}\right]=\mu\frac{\partial^2 u}{\partial z^2} \tag{9}$$

$$\frac{\partial p}{\partial y}=\frac{\partial}{\partial z}\left[\mu\frac{\partial v}{\partial z}\right]=\mu\frac{\partial^2 v}{\partial z^2} \tag{10}$$

$$\frac{\partial p}{\partial z}=0 \tag{11}$$

Where, u, v, w indicate the velocity in x, y, z directions respectively，p is dynamic pressure, μ is the dynamic viscosity of the polishing slurry. Considering the small working gaps, the thickness of the wedge gap area can be seen as a thin layer, fluid behavior can be well approximated using Reynolds equation [80] combined with viscosity changes. Specifically, the Reynolds equation in the working gaps, pressure p, slurry thickness h and viscosity μ can be expressed as

$$\frac{\partial}{\partial x}\left(\frac{h^3\cdot\partial p}{\partial x}\right)+\frac{\partial}{\partial y}\left(\frac{h^3\cdot\partial p}{\partial y}\right)=6\mu\left[u\frac{\partial h}{\partial x}+v\frac{\partial h}{\partial y}\right] \tag{12}$$

According to the constitutive equation of non-Newtonian power-law fluids [81]

$$\mu=k\cdot|\dot{\gamma}|^{n-1} \tag{13}$$

Where k is the consistency constant and n is the flow index.

Then the shear rate can be expressed as [76]

$$\tau=\mu\cdot|\gamma|=k\cdot|\gamma|^{n} \tag{14}$$

Where, γ is the velocity gradient, defined as [82] $\gamma=\nabla V=\partial V/\partial h$, $V=\sqrt{u^2+v^2}$ is the sum velocity of the xy plane.

Slurry thickness h can be defined as [83]

$$h(x, y) = R - \sqrt{R^2 - x^2} + d \tag{15}$$

Where, R is the radius of the polishing tool and d is the polishing gap.

By iterative calculation with the discrete differential algorithm and Reynolds equation, the stable convergent pressure can be obtained. Subsequently, the equivalent principal stress P_p considering the shear stress could be calculated according to the von-Mises criterion.

Appendix B. Size parameters related to profiling damping tool fabrication

Fig. B.20 illustrates the relevant dimensional parameters for the design of the profiling tool. The groove depth of the profiling damping tool is 0.4 mm. During the production of the replication film, there is a 0.2 mm gap between the outer circle of the tool substrate and the upper surface of the workpiece, which means that there is a 0.6 mm gap between the bottom of the shaped tool groove and the upper surface of the workpiece. This precisely matches the thickness of the damping polishing pad, ensuring that the surface of the polishing pad on the shaped tool aligns perfectly with the lowest end of the replication film, without affecting the polishing process.

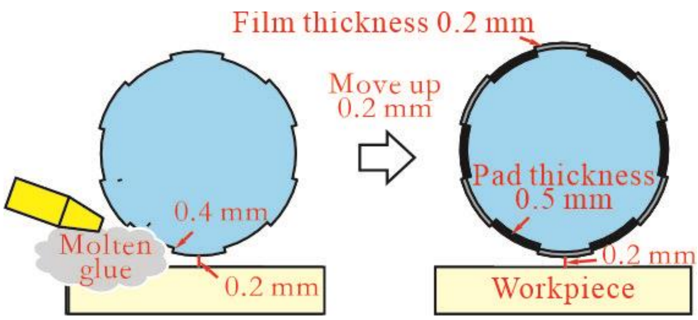

Fig. B.20. Dimensional information relevant to the replication film production process

References:

[1] Kong L, Cheung CF. Design, fabrication and measurement of ultra-precision micro-structured freeform surfaces. Comput Ind Eng 2011;61:216-225.

[2] Sanmartin DR, Zhang D, Button T, Atkins C, Doel P, Wang H, Brooks D, Feldman C, Willingale R, Michette A. Progress on the development of active micro-structured optical arrays for X-ray optics. Advances in X-Ray/EUV Optics and Components IV, SPIE 2009:67-76.

[3] McDonald AT, Fox RW. An experimental investigation of incompressible flow in conical diffusers. Int J of Mech Sci 1966;8:125-139.

[4] Zhu WL, Duan F, Zhang X, Zhu Z, Ju BF. A new diamond machining approach for extendable fabrication of micro-freeform lens array. Int J Mach Tool Manu 2018;124:134-148.

[5] Wu H, Odom TW, Whitesides GM. Reduction photolithography using microlens arrays: applications in gray scale photolithography. Anal. Chem 2002;74:3267-3273.

[6] Lee J, Park J, Park CW, Cho SH, Kim YY. Uni-modal retroreflection in multi-modal elastic wave fields. Int J Mech Sci 2022;232:107655.

[7] Antonakakis T, Craster RV, Guenneau S, Skelton EA. An asymptotic theory for waves guided by diffraction gratings or along microstructured surfaces. P Roy Soc A-Math Phy 2014;470:20130467.

[8] Chen EG, Xie HX, Huang JM, Miu HH, Shao GR. Flexible/curved backlight module with quantum-dots microstructure array for liquid crystal displays. Opt Express 2018;3:3466-3482.

[9] Wu YT, Zhang L, Ge PQ, Gao YF, Bi WB. Effects of the micro-structure of arc-shaped groove, rectangular groove and semicircle-based rectangular groove on the reflectance of silicon solar cell. Sol Energy 2017;158:617-625.

[10] Boneberg J, Leiderer P. Optical near-field imaging and nanostructuring by means of laser ablation. 2022;1:210003.

[11] Stevens R, Harvey T. Lens arrays for a three-dimensional imaging system. J Opt A-Pure Appl Op 2002;4:S17.

[12] Xiao JS, Liu J, Han J, Wang YT. Design of achromatic surface microstructure for near-eye display with diffractive waveguide. Opt Commun 2019;452:411-416.

[13] Yang L, El-Tamer A, Hinze U, Li J, Hu Y, Huang W, Chu J, Chichkov BN. Parallel direct laser writing of micro-optical and photonic structures using spatial light modulator. Opt Laser Eng 2015;70:26-32.

[14] Lehmann P, Xie WC, Niehues J. Transfer characteristics of rectangular phase gratings in interference microscopy. Opt lett 2012;37:758-760.

[15] Ghebjagh SG, Handte T, Sinzinger S. Micro-diffractive optical element arrays for beam shaping. in: European Physical Journal Web of Conferences 2022:13013.

[16] Zhang ZL, Wang CJ, Zhu WL, Guo J, Cheung CF. Surface generation modelling and form maintenance strategy in maskless fluid jet polishing of structured array surface. Appl Surf Sci 2023;622:156855.

[17] Cirino GA, Granado RM, Mohammed BT, Jasinevicius RG. Assessment of replication fidelity of optical microstructures by hot embossing. Int J Adv Manuf Tech 2017;88:303-316.

[18] Shu CS, Guo XP, Yin SH, Huang S, Mao ZZ. Fabrication of curved aspheric compound eye microlens array with high surface quality by precision glass molding. Precis Eng 2023;82:129-139.

[19] Zhang YY, Liang RG, Spires OJ, Yin SH, Yi A, Milster TD. Precision glass molding of diffractive optical elements with high surface quality. Opt Lett 2020;45:6438-6441.

[20] Huang YT, Li SJ, Zhang J, Yang C, Liu WG. Research on shape error of microstructure array fabricated by fly cutting. Optik 2021;241:167031.
[21] Zhang SJ, Zhou YP, Zhang HJ, Xiong ZW, To S. Advances in ultra-precision machining of micro-structured functional surfaces and their typical applications. Int J Mach Tool Manu 2019;142:16-41.
[22] Guo B, Zhao QL, Fang XY. Precision grinding of optical glass with laser micro-structured coarse-grained diamond wheels. J Mater Process Tech 2014;214:1045-1051.
[23] Aurich JC, Kirsch B, Setti D, Axinte D, Beaucamp A, Butler SP, Yamaguchi H. Abrasive processes for micro parts and structures. CIRP Annals 2019;68:653-676.
[24] Dong XW, Guo L, Bo W, Zheng Q, Lei L. Fabrication of Microstructured Surfaces by Five-Axis Ultra Precision Machine Tool. Key Eng. Mater. (Switzerland) 2015;625:187-191.
[25] Zhou TF, Xu RZ, Ruan BS, He YP, Liang ZQ, Wang XB. Study on new method and mechanism of microcutting-etching of microlens array on 6H-SiC mold by combining single point diamond turning with ion beam etching. J Mater Process Tech 2020;278:116510.
[26] Jiang JK, Luo T, Zhang GQ, Dai YQ. Novel tool offset fly cutting straight-groove-type micro structure arrays. J Mater Process Tech 2021;288.
[27] Guo J, Zhang J, Wang H, Liu K, Kumar AS. Surface quality characterisation of diamond cut V-groove structures made of rapidly solidified aluminium RSA-905. Precis Eng 2018;53:120-133.
[28] Huang YT, Fan B, Wan YJ, Li SJ. The research of single point diamond turning Fresnel lens technology. the 9th International Symposium on Advanced Optical Manufacturing and Testing Technologies: Micro-and Nano-Optics, Catenary Optics, and Subwavelength Electromagnetics, SPIE 2019:241-248.
[29] Wang H, To S, Chan C, Cheung CF, Lee WB. A theoretical and experimental investigation of the tool-tip vibration and its influence upon surface generation in single-point diamond turning. Int J Mach Tool Manu 2010;50:241-252.
[30] Wing BL, Ling BK, Chi FC, Suet T, Xin C, Qiang L. An overview of ultra-precision diamond machining of microstructured freeform surfaces. J Mech Eng 2013;49:144-155.
[31] Ma Y, Zhang G, Cao S, Huo Z, Han J, Ma S, Huang Z. A Review of Advances in Fabrication Methods and Assistive Technologies of Micro-Structured Surfaces. Processes 2023;11:1337.
[32] Tamkin JM, Milster TD. Effects of structured mid-spatial frequency surface errors on image performance. Appl Optics 2010;49:6522-6536.
[33] Zhou K, Ding HH, Wang RX, Yang JY, Guo J, Liu QY, Wang WJ. Experimental investigation on material removal mechanism during rail grinding at different forward speeds. Tribol Int 2020;143:106040.
[34] Zhou TF, Zhou J, Chen HL, Wang ZF, Ruan BS, Zhao WX, Wang XB. Study of diffractive fringes caused by tool marks for fast axis collimators fabricated by precision glass molding. Opt Express 2022;30:26581-26596.
[35] Zheng XT, Wei HL, Li SB, Wu DM, Liu Y, Zhang YJ, Xu H, Zhou Y. The research on structure design of LED fluorescent lamp microstructures diffuser and the effect on the optical properties. Advanced Materials Research 2013;712:1274-1278.
[36] Brinksmeier E, Riemer O, Stern R. Machining of precision parts and microstructures, in: Initiatives of Precision Engineering at the Beginning of a Millennium. Springer 2002:3-11.
[37] Brinksmeier E, Riemer O, Gessenharter A. Finishing of structured surfaces by abrasive polishing. Precis Eng 2006;30:325-336.

[38] Wang CJ, Cheung CF, Ho LT, Liu MY, Lee WB. A novel multi jet polishing process and tool for high-efficiency polishing. Int J Mach Tool Manu 2017;115:60-73.
[39] Wang CJ, Mou XY, Luo W, Lu YJ. Precision Grinding and Polishing of Optical Micro-structured Surface, in: Fabrication of Micro/Nano Structures via Precision Machining: Modelling, Processing and Evaluation. Springer 2023:337-360.
[40] Wang CJ, Zhang ZL, Cheung CF, Luo W, Loh YM, Lu YJ, Kong LB, Wang SX. Maskless fluid jet polishing of optical structured surfaces. Precis Eng 2022;73:270-283.
[41] Guo J, Kum CW, Au KH, Wu H, Liu K. New vibration-assisted magnetic abrasive polishing (VAMAP) method for microstructured surface finishing. Opt Express 2016;24:13542-13554.
[42] Guo J, Jong HJH, Kang RK, Guo DM. Novel localized vibration-assisted magnetic abrasive polishing method using loose abrasives for V-groove and Fresnel optics finishing. Opt Express 2018;26:11608-11619.
[43] Huang H, Qian YF, Zhang L, Jiang MQ, Yan JW. A novel method for fabricating micro-dimple arrays with good surface quality on metallic glass substrate by combining laser irradiation and mechanical polishing under wax sealing. J Manuf Process 2022;79:911-923.
[44] Zhang C, Chen LY, Wang G, Jin J, Zhang YK. Effects of laser processing crater array microstructure on the surface characteristics and bonding strength of Ti6Al4V adhesive joints. Opt Laser Technol 2021;141:107125.
[45] Liu XH, Zhou TF, Zhou WC, Yi A, Liang ZQ, Wang XB. Modeling and experiment of concave microlens array on silicon wafer by grinding-polishing process with diamond slurry, in: Sixth Asia Pacific Conference on Optics Manufacture, SPIE 2020:62-70.
[46] Kumar P, Son SY, Lee J, Chang FC, Khanna A, Arjunan AC, Singh RK. Microlens array fabrication by chemical mechanical polishing. Electrochem Solid St 2009;12:H269.
[47] Zhao QL, Sun ZY, Guo B. Material removal mechanism in ultrasonic vibration assisted polishing of micro cylindrical surface on SiC. Int J Mach Tool Manu 2016;103:28-39.
[48] Sun ZG, Fan ZH, Tian YB, Prakash C, Guo J, Li L. Post-processing of additively manufactured microstructures using alternating-magnetic field-assisted finishing. J Mater Res Technol 2022;19:1922-1933.
[49] Wang CJ, Cheung CF, Liu MY, Lee WB. Fluid jet-array parallel machining of optical microstructure array surfaces. Opt Express 2017;25:22710-22725.
[50] Chen FJ, Hao SM, Miao XL, Yin SH, Huang S. Numerical and experimental study on low-pressure abrasive flow polishing of rectangular microgroove. Powder Technol 2018;327:215-222.
[51] Zhu WL, Beaucamp A. Non-Newtonian fluid based contactless sub-aperture polishing. CIRP Annals 2020;69:293-296.
[52] Zhu WL, Gao W, Han F, Ju BF, Chen YL, Beaucamp A. Compliant polishing of thin-walled freeform workpiece. CIRP Annals 2023.
[53] Li M, Lyu BH, Yuan JL, Dong CC, Dai WT. Shear-thickening polishing method. Int J Mach Tool Manu 2015;94:88-99.
[54] Lyu BH, Shao Q, Hang W, Chen SH, He QK, Yuan JL. Shear thickening polishing of black lithium tantalite substrate. Int J Precis Eng Man 2020;21:1663-1675.
[55] Li M, Song FZ, Huang ZR. Control strategy of machining efficiency and accuracy in weak-chemical-coordinated-thickening polishing (WCCTP) process on spherical curved 9Cr18 components. J Manuf Process 2022;74:266-282.
[56] Wang JH, Zhou Y, Qiao Z, Goel S, Wang JH, Wang X, Chen HY, Yuan JL, Lyu BH. Surface

polishing and modification of Ti-6Al-4V alloy by shear thickening polishing. Surf Coat Tech 2023;468:129771.

[57] Zhou DD, Huang XM. Ming Y, Li XY, Li HY, Li W, Material removal characteristics of magnetic-field enhanced shear thickening polishing technology. J Mater Res Technol, 2021;15:2697-2710.

[58] Li M, Liu MH, Riemer O, Song FZ, Lyu BH. Anhydrous based shear-thickening polishing of KDP crystal. Chinese J Aeronaut 2021;34:90-99.

[59] Zhang PF, Li LG, Yang Z, Pan B, Zhang M, Guo XG, Li G, Kim DW, Guo J. Achieving sub-nanometer roughness on aspheric optical mold by non-contact polishing using damping-clothed tool. Opt Express 2022;30:28190-28206.

[60] Wang JH, Lyu BH, Jiang L, Shao Q, Deng CB, Zhou YF, Wang JH, Yuan JL. Chemistry enhanced shear thickening polishing of Ti–6Al–4V. Precis Eng 2021;72:59-68.

[61] Li M, Lyu BH, Yuan JL, Yao WF, Zhou FF, Zhong MP. Evolution and equivalent control law of surface roughness in shear-thickening polishing. Int J Mach Tool Manu 2016;108:113-126.

[62] Nguyen DN. Simulation and experimental study on polishing of spherical steel by non-Newtonian fluids. Int J Adv Manuf Tech 2020;107:763-773.

[63] Shao Q, Lyu BH, Yuan JL, Wang X, Ke MF, Zhao P. Shear thickening polishing of the concave surface of high-temperature nickel-based alloy turbine blade. J Mater Res Technol 2021;11:72-84.

[64] Zhu ZH, Huang P, To S, Zhu LM, Zhu Z. Fast-tool-servo-controlled shear-thickening micropolishing. Int J Mach Tool Manu. 2023;184:103968.

[65] Li ZZ, Wang JM, Peng XQ, Ho L, Yin Z, Li S, Cheung CF. Removal of single point diamond-turning marks by abrasive jet polishing. Appl Optics 2011;50:2458-2463.

[66] Wei HB, Gao H, Wang XY. Development of novel guar gum hydrogel based media for abrasive flow machining: Shear-thickening behavior and finishing performance. Int J Mech Sci 2019;157:758-772.

[67] Wei MH, Lin K, Sun L. Shear thickening fluids and their applications. Mater Design 2022;216:110570.

[68] Xie ZL, Ta N, Rao ZS. The lubrication performance of water lubricated bearing with consideration of wall slip and inertial force. J Hydrodyn. Ser. B 2017;29:52-60.

[69] Roesle M, Coskun V, Steinfeld A, Numerical analysis of heat loss from a parabolic trough absorber tube with active vacuum system. 2011.

[70] Jünemann T, Pleskun H, Brümmer A. Maxwell velocity slip and Smoluchowski temperature jump boundary condition for ANSYS CFX. IOP Conference Series: Materials Science and Engineering, 2021:012037.

[71] Zhang ZF, Zhang YL. Finite element simulation of extrusion of optical fiber preforms: Effects of wall slip. Opt Fiber Technol 2016;28:18-22.

[72] Jeong W, Seong J. Comparison of effects on technical variances of computational fluid dynamics (CFD) software based on finite element and finite volume methods. Int J Mech Sci 2014;78:19-26.

[73] Pan R, Zhao WY, Zhong B, Chen DJ, Wang ZZ, Zha CQ, Fan JW. Evaluation of removal characteristics of bonnet polishing tool using polishing forces collected online. J Manuf Process 2019;47:393-401.

[74] Ke XL, Wang CJ, Guo YB, Xu Q. Modeling of tool influence function for high-efficiency polishing. Int J Adv Manuf Tech 2016;84:2479-2489.

[75] Ali D, Sen S. Finite element analysis of mechanical behavior, permeability and fluid induced wall shear stress of high porosity scaffolds with gyroid and lattice-based architectures. J Mech Behav Biomed 2017;75:262-270.
[76] Zhou DD, Huang XM, Ming Y, Li XY, Li HY, Li W. Material removal characteristics of magnetic-field enhanced shear thickening polishing technology. J Mater Res Technol 2021;15:2697-2710.
[77] Lu A, Guo K, Jin T, Liu QF. Modeling and experimentation of dynamic material removal characteristics in dual-axis wheel polishing. Int J Mech Sci 2019;151:523-536.
[78] Zhang J, Wang H. Generic model of time-variant tool influence function and dwell-time algorithm for deterministic polishing. Int J Mech Sci 2021;211:106795.
[79] Zhu WL, Beaucamp A. Generic three-dimensional model of freeform surface polishing with non-Newtonian fluids. Int J Mach Tool Manu 2022;172:103837.
[80] Marušić PE, Marušić S. Analysis of the Reynolds equation for lubrication in case of pressure-dependent viscosity. Math Probl Eng 2013.
[81] Li M, Karpuschewski B, Ohmori H, Riemer O, Wang Y, Dong T. Adaptive shearing-gradient thickening polishing (AS-GTP) and subsurface damage inhibition. Int J Mach Tool Manu 2021;160:103651.
[82] Ming Y, Huang X, Zhou D, Li X. A novel Non-Newtonian fluid polishing technique for zirconia ceramics based on the weak magnetorheological strengthening thickening effect. Ceram Int 2022;48:7192-7203.
[83] Zhu WL, Achour SB, Beaucamp A. Centrifugal and hydroplaning phenomena in high-speed polishing. CIRP Annals 2019;68:369-372.